The Astrophysical Journal, 912:141 (15pp), 2021 May 10 https://doi.org/10.3847/1538-4357/abf143

Simulating the Solar Minimum Corona in UV Wavelengths with Forward Modeling II. Doppler Dimming and Microscopic Anisotropy Effect

Jie Zhao (赵洁)[1,2,7], Sarah E. Gibson[2,7], Silvano Fineschi[3], Roberto Susino[3], Roberto Casini[2,7], Steven R. Cranmer[4], Leon Ofman[5,6], and Hui Li (黎辉)[1]

[1] Key Laboratory of Dark Matter and Space Astronomy, Purple Mountain Observatory, Chinese Academy of Sciences, Nanjing, Jiangsu, People's Republic of China
zhaojie@pmo.ac.cn
[2] National Center for Atmospheric Research, 3080 Center Green Dr., Boulder, CO 80301, USA
[3] INAF - Turin Astrophysical Observatory, I-10025 Pino Torinese (TO), Italy
[4] Department of Astrophysical and Planetary Sciences, Laboratory for Atmospheric and Space Physics, University of Colorado, Boulder, CO 80309, USA
[5] Catholic University of America, Washington, DC 20064, USA
[6] NASA Goddard Space Flight Center, Code 671, Greenbelt, MD 20771, USA
Received 2020 September 8; revised 2021 March 10; accepted 2021 March 22; published 2021 May 14

Abstract

In ultraviolet (UV) spectropolarimetric observations of the solar corona, the existence of a magnetic field, solar wind velocity, and temperature anisotropies modify the linear polarization associated with resonant scattering. Unlike previous empirical models or global models, which present blended results of the above physical effects, in this work, we forward-model expected signals in the H I Lyα line (121.6 nm) by adopting an analytic model that can be adjusted to test the roles of different effects separately. We find that the impact of all three effects is most evident in the rotation of the linear polarization direction. In particular, (1) for magnetic fields between ~10 and ~100 G, the Hanle effect modifies the linear polarization at low coronal heights, rotating the linear polarization direction clockwise (counterclockwise) when the angle between the magnetic field and the local vertical is greater (less) than the van Vleck angle, which is consistent with the result of Zhao et al.; (2) solar wind velocity, which increases with height, has a significant effect through the Doppler dimming effect at higher coronal heights, rotating the linear polarization direction in an opposite fashion to the Hanle effect; and (3) kinetic temperature anisotropies are most significant at lower heights in open nonradial magnetic field regions, producing tilt opposite to isotropic Doppler dimming. The fact that the three effects operate differently in distinct spatial regimes opens up the possibility for using linear polarization measurements in UV lines to diagnose these important physical characteristics of the solar corona.

Unified Astronomy Thesaurus concepts: Solar wind (1534); Coronagraphic imaging (313); Solar ultraviolet emission (1533)

1. Introduction

The solar corona lies at the heart of many of the unsolved problems in solar physics. How is it heated to a million degrees? How is it accelerated to expand outwards as the solar wind? What are the processes controlling coronal mass ejections and flare? And the overarching question for all of these: what is the structure and topology of the coronal magnetic field?

Until now, the most prevalent method of obtaining the coronal magnetic field is from the extrapolation of photospheric magnetograms, under various assumptions such as a magnetically dominated, or force-free field. Data-driven MHD simulations incorporate the extrapolated magnetic field and obtain the evolution of the complete physical state. They are successful in reproducing eruptive events—for example, qualitative similarities are found between the topology of the magnetic field (as determined e.g., from quasi-separatrix layers Titov & Démoulin 1999; Titov et al. 2002) and the morphology of flare ribbons. However, to investigate such events quantitatively, direct measurement of the coronal magnetic field is necessary. The Zeeman effect has been widely used to measure the strong magnetic field at the photosphere, but measurement in the corona has been rarer (Lin et al. 2004). Another option is to use the Hanle effect to probe magnetic field topology (Bąk-Stęślicka et al. 2013; Gibson et al. 2017) and strength (Bommier & Sahal-Bréchot 1982; Sahal-Bréchot et al. 1986; Fineschi et al. 1991; Zhao et al. 2019, and references therein.).

The investigation of solar wind acceleration is also of critical importance. In the era of the Solar and Heliospheric Observatory (SOHO; Domingo et al. 1995), solar wind velocity has been measured by the Ultraviolet Coronagraph Spectrometer (UVCS; Kohl et al. 1995) through the Doppler dimming effect.

One of the discoveries of SOHO was the anisotropy of the microscopic velocity (i.e., kinetic temperature), first announced by Kohl et al. (1997), through the estimated temperature of the heavy ion O^{5+} in the solar wind. This analysis found that the line width is much wider perpendicular to the magnetic field than along the magnetic field, indicating that the kinetic temperature is higher in the perpendicular direction.

The magnetic field, Doppler dimming effect, and temperature anisotropy of the solar wind have been extensively studied in observations (e.g., Kohl et al. 1998; Li et al. 1998; Antonucci et al. 2000; Raouafi et al. 2002b; Antonucci et al. 2012; Bąk-Stęślicka et al. 2013; Dolei et al. 2016) and in numerical calculations (e.g., Bommier & Sahal-Bréchot 1982; Sahal-Bréchot et al. 1986; Fineschi et al. 1991, 1993, 1999; Davila & Ofman 1999; Gary et al. 2001, 2003; Ofman & Davila 2001; Ofman et al. 2001, 2005, 2014; Raouafi et al. 2002a; Li et al. 2004; Raouafi & Solanki 2006; Sahal-Bréchot & Raouafi 2006; Ofman & ViñAs 2007; Ofman 2010;

[7] The National Center for Atmospheric Research is sponsored by the National Science Foundation.

Khan et al. 2011; Khan 2012; Khan & Landi Degl'Innocenti 2012; Maneva et al. 2013, 2015).

To diagnose the physical state of the corona (such as the magnetic field, solar wind velocity, and temperature anisotropy as discussed above), routine spectropolarimetric observations are desired. However, the problem of inversion is nontrivial. The magnetic field, solar wind velocity, and temperature anisotropy exist simultaneously in the corona and modify both the direction and magnitude of the linear polarization in different ways. The primary purpose of this work is to show the working regime of different effects and to provide insight for understanding future observations. To achieve this goal, we learn the roles separately and jointly by adopting an analytic model that can be adjusted to turn on or off the above effects without changing the values to probe sensitivities to the different effects. Moreover, the present model employs an analytic 3D axisymmetric magnetic field structure, providing a more realistic model of the solar corona than 1D models.

In this work, we extend our forward-modeling analysis of the Hanle effect by considering the impact of the magnetic field, solar wind velocity, and anisotropy of the microscopic velocity on the polarization profile of ultraviolet (UV) emission lines in order to demonstrate the diagnostic ability of these lines. In Section 2, we describe the symmetry-breaking processes that affect polarization. In Section 3, we describe a global coronal-hole/streamer model appropriate for describing the solar minimum corona (Gibson et al. 1996). Our results are shown in Section 4, and we discuss our conclusions in Section 5.

2. Polarization and Symmetry-breaking Processes

Resonant scattering producing linear polarization takes place in the corona, and changes to the physical state of the ions (scatterers) in the corona will modify the polarized light. In the following, we introduce three aspects that may affect linear polarization.

2.1. Magnetic Field

The symmetry-breaking process induced by the nonradial magnetic field is through the so-called Hanle effect, which modifies the magnitude of the linear polarization and rotates the direction of the linear polarization. A detailed study on the Hanle effect can be found in Zhao et al. (2019, hereafter Paper I).

2.2. Solar Wind

The slow solar wind is associated with the edges of coronal streamers and other possible sources in the corona (Abbo et al. 2016 and references therein), and fast solar wind emerges from coronal holes (e.g., McComas et al. 2008). The solar wind follows the magnetic field direction in the lower corona because magnetic forces dominate (low plasma β). However, the speed of solar wind increases and magnetic field strength decreases with heliocentric distance, and the solar wind ultimately dominates, pulling the magnetic field out radially. Nevertheless, the field and flow stay aligned because of the high degree of ionization and the frozen-in near-ideal plasma condition.

The amplitude of scattered intensity (both polarized and unpolarized) will decrease in the wing of the incident radiation line: this is the so-called Doppler dimming effect (Hyder & Lites 1970; Beckers & Chipman 1974). When we integrate the polarized light through a solid angle that is subtended by the incident radiation, the magnitude of the intensity and linear polarization will decrease, but the direction of the linear polarization will remain the same when the velocity is along the radial direction (assuming cylindrically symmetric incident radiation). When the velocity is nonradial, the effect is larger, and the direction of the linear polarization will rotate compared to the case with radial velocity.

Doppler dimming is illustrated in Figure 1, panels (a) and (b). Panel (a) shows the case with zero or radial velocity (along radial magnetic field). Here, both the unpolarized and the polarized line intensity amplitudes will decrease due to the Doppler dimming effect, but the linear polarization direction will not change but stay parallel to the solar limb (assuming zero magnetic field) because the resonant scattering is symmetric. Panel (b) shows the case with nonradial velocity (along a nonradial magnetic field)—the Doppler dimming effect will be more prominent along the direction of the bulk velocity than in other directions, and so linear polarization will be decreased in this direction. Hence, the integral of the linear polarization over solid angle will result in a rotation of the linear polarization toward the direction where the solar wind velocity is maximal because the resonant scattering is no longer symmetric.

2.3. Anisotropic Distribution of Microscopic Velocity

UVCS found the anisotropic distribution of microscopic velocity in the solar wind as well as in streamers during solar minimum (see Kohl et al. 2006; Antonucci et al. 2012, and references therein), which implied that the thermal temperature along the magnetic field is different from (smaller than) the one perpendicular to the magnetic field for the H I Lyα and O VI UV lines. Cranmer et al. (1999) used these observations to design an empirical model on the solar wind anisotropy, which has been improved in Cranmer et al. (2008). Additional understanding of the origin of this anisotropy has come from a wide range of studies of collisionless wave-particle interactions (e.g., Cranmer 2001, 2014; Ofman et al. 2001; Tu & Marsch 2002; Chandran et al. 2010; Isenberg et al. 2019). These kinetic theories and models (Gary et al. 2001; Ofman et al. 2001, 2002) suggested that once the ion temperature anisotropy ($T_\perp/T_\parallel$) reaches a threshold of $\sim$10 for the typical plasma beta values in the solar wind, the instability will transform the energy from the perpendicular to the parallel direction, making the solar wind more isotropic.

Empirical models fit to observations indicate that the O^{5+} ion temperature anisotropy factor ($T_\perp/T_\parallel$) in the fast solar wind is much greater than in the streamer (Abbo et al. 2016). This effect is much greater for O VI than for H I Lyα. This is illustrated in Figure 1, panel (c). The anisotropy of the kinetic temperature in the solar wind results in a broader line profile in the perpendicular direction than in the parallel direction. The resonant scattering then is more effective in the parallel direction than in the perpendicular direction. The linear polarization induced by the resonant scattering will be asymmetric for the integral, resulting in a rotation of the polarization toward the direction where the kinetic temperature is larger and the line width is bigger.

The Doppler dimming effect (panel (b)) and the anisotropic effect (panel (c)) are expected to occur together in the anisotropic solar wind. Figure 1, panel (d), shows such a combination of these two effects. As we mentioned above, the

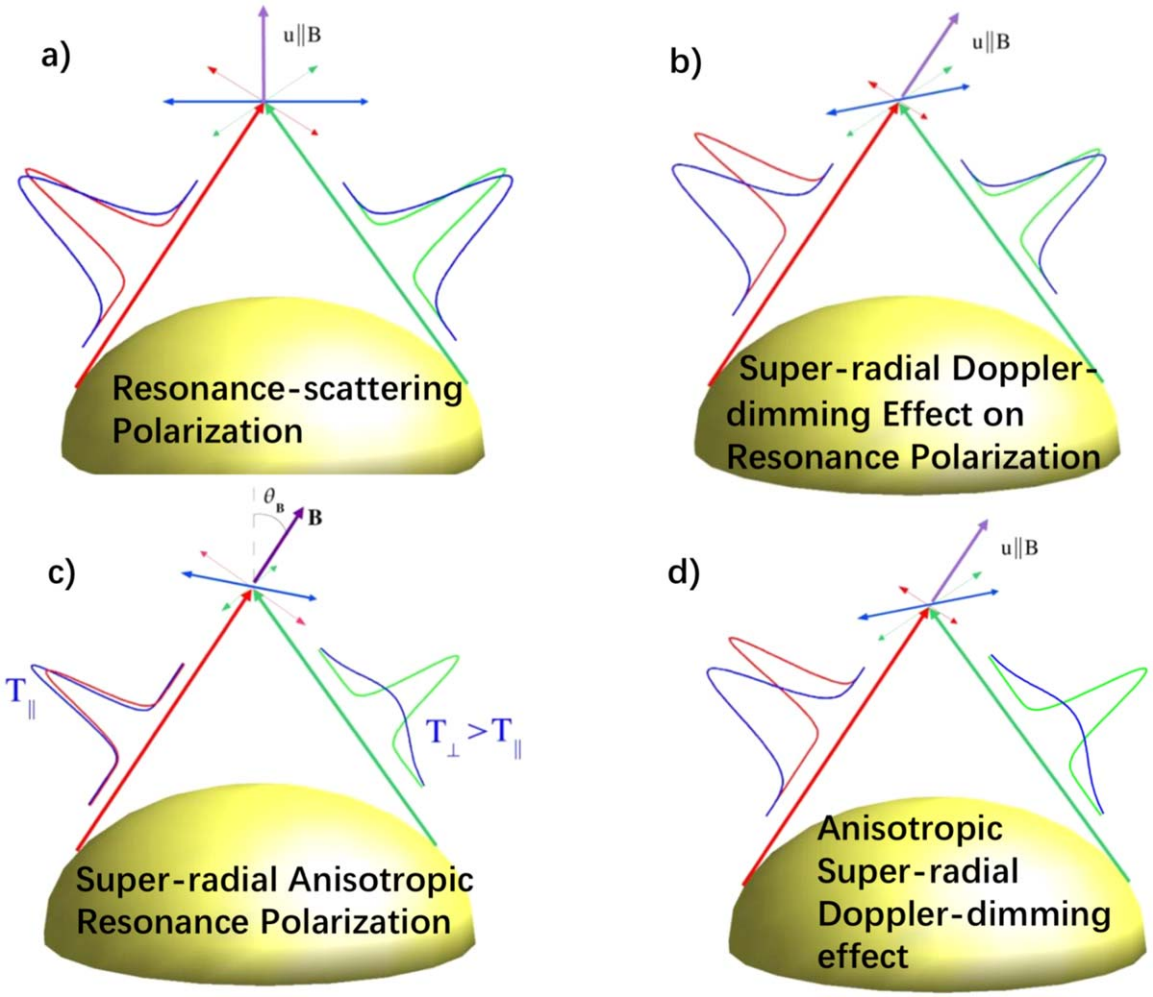

Figure 1. Sketch for the physical processes—not connected to the Hanle effect—that result in the polarization vector's rotations studied in this work (see Fineschi 2001). (a) Zero-field, zero-wind, incident radiation (red/green spectra) resonantly scatters with coronal ions (blue spectra), and the polarization vector observed from a line of sight perpendicular to the page results from the vector sum of all the polarization vectors of the scattered rays coming from the underlying chromospheric cap. (b) Nonradial wind velocities break the symmetry of the radial resonance scattering process so that even with a negligible field strength (i.e., no Hanle effect), there is a rotation of the polarization vector. (c) Collisionless kinetic effects introduce an anisotropy in the ion microscopic velocity distribution where the Doppler dimming—not due to the wind speed—also rotates the polarization vector. (d) Both effects due to nonradial wind velocities and kinetic temperature anisotropies can occur together

Doppler dimming effect results in a rotation of the linear polarization toward the direction of the maximum solar wind, while the anisotropic effect results in a rotation toward the direction of maximum anisotropy. Thus, the combination of these two effects can be complex.

2.4. Assumptions and Equations

The equations that we use to calculate the polarization state in this paper are basically the same as those used in Sections 2.1 and 2.2 of Khan et al. (2011, hereafter referred to as Paper II). A two-level atomic model is assumed, with an unpolarized lower level, whose upper level has either $J_u = 3/2$ or $J_u = 1/2$ and the lower level has $J_u = 1/2$. This is a viable assumption for the H I Lyα system studied here because the ground state of hydrogen cannot harbor any atomic alignment (when hyperfine structure effects can be ignored; e.g., see Bommier & Sahal-Bréchot 1982). Also, because of the large coronal temperature and the spectral width of the H I Lyα line excitation from below, the width of the absorption profile in the atom rest frame can be assumed to be virtually a Dirac delta function, and therefore, we also make the assumption of "infinitely" sharp lower and upper levels in the atomic frame. Based on these assumptions, we follow the two-level atom treatment described by Landi Degl'Innocenti (1984), which has the advantage of giving analytical expressions for the Stokes parameters' line emissivity from a two-level atom, in the limiting case of complete depolarization of the ground level, and in the presence of a magnetic field. The Stokes parameters of the line emissivity, $\epsilon_i(\mathbf{\Omega})$ $(i = 0, 1, 2, 3)$, along the direction $\mathbf{\Omega}$, are given by Equation (3) in Paper II:

$$\epsilon_i(\mathbf{\Omega}) = k_L^A \sum_{KQ} W_k(J_l, L_u)(-1)^Q \mathcal{T}_Q^K(i, \mathbf{\Omega}) J_{-Q}^K(\nu_0) \times (i = 0, 1, 2, 3), \quad (1)$$

where k_L^A is the frequency-integrated absorption coefficient of the line, given by $k_L^A = \frac{h\nu}{4\pi}\mathcal{N}B(\alpha_l J_l \rightarrow \alpha_u J_u)$, with $B(\alpha_l J_l \rightarrow \alpha_u J_u)$ being the Einstein coefficient for absorption from the lower to the upper energy levels, respectively. The energy of the scattered

photons is $h\nu$, and $\mathcal{N}_l = \mathcal{N}\sqrt{2J_l+1}\,\rho^0_0(\alpha_l J_l)$ is the number of hydrogen atoms per unit volume in the lower level, $\mathcal{N}$ being the overall number density of atoms. The multipole moment of the unpolarized lower level, $\rho^0_0(\alpha J)$, is proportional to the number density of hydrogen atoms, and α is a set of quantum numbers related to the spectroscopic properties of the energy level (see Paper II). The tensor J^K_Q describes the incoming radiation field. It is usually called the radiation field tensor (see Paper II). The frequency ν_0 corresponds to the line transition between the upper and lower energy levels. Finally, $W_K(J_l, J_u) = [w^{(K)}_{J'J}]^2$ is a sort of "efficiency factor" characterizing the transfer of the Kth-order multipole moment from the radiation field to the atomic density matrix in the absorption process from the lower to the upper level. This factor is defined in Equation (63) of Landi Degl'Innocenti (1984), where Table 1 also lists its numerical values. Appendix 1 of the same reference summarizes the expressions and the properties of the irreducible tensors of the polarization unit vectors $\mathcal{T}^K_Q(i, \boldsymbol{\Omega})$.

The radiation tensor J^K_Q contains the irreducible tensors of the polarization unit vectors, $\mathcal{T}^K_Q(j, \boldsymbol{\Omega}')$, describing the geometry of the radiation field incoming from direction $\boldsymbol{\Omega}'$ and in terms of the jth Stokes parameters (see Equation (64) in Landi Degl'Innocenti 1984). In this way, the geometry of the incoming radiation from the direction $\boldsymbol{\Omega}'$ and that of the scattered radiation into the direction $\boldsymbol{\Omega}$ can be expressed as a combination of the two irreducible tensors of the polarization unit vectors for the incoming and scattered photons:

$$P_{ij}(\boldsymbol{\Omega}, \boldsymbol{\Omega}') = \sum_{KQ} W_K(J, J')(-1)^Q \mathcal{T}^K_Q(i, \boldsymbol{\Omega}) \mathcal{T}^K_{-Q}(j, \boldsymbol{\Omega}'). \quad (2)$$

This equation is the classical expression of the scattering phase matrix, which relates the radiation scattered into direction $\boldsymbol{\Omega}$ to the incident radiation from direction $\boldsymbol{\Omega}'$. In the presence of a magnetic field vector, $\boldsymbol{B}$, the expression of the Hanle effect scattering phase matrix becomes (see Equation (17) in Landi Degl'Innocenti 1985):

$$P_{ij}(\boldsymbol{\Omega}, \boldsymbol{\Omega}') = \sum_{KQ} W_K(J, J')(-1)^Q \mathcal{T}^K_Q(i, \boldsymbol{\Omega}) \times \cos\alpha_Q\, e^{-i\alpha_Q} \times \mathcal{T}^K_{-Q}(j, \boldsymbol{\Omega}'), \quad (3)$$

where $\alpha_Q (Q = -2, ..., 2)$ are the quantities implicitly defined by $\tan\alpha_Q = \gamma Q$. The critical parameter for the appearance of the Hanle effect is $\gamma = 0.88B\, g_{J_u}/A(J_u, J_l)$, where g_{J_u} is the Landé factor of the upper level, the field B is in Gauss, and $A(J_u, J_l)$ is the Einstein coefficient for the spontaneous emission in units of $10^{-7}\,\mathrm{s}^{-1}$.

The analytical expression of the Hanle effect scattering phase matrix is adopted from Landi Degl'Innocenti & Landi Degl'Innocenti (1988). The incident radiation, which has a line width of 0.4 Å, is assumed to be unpolarized and independent of the heliocentric angle. This is also a reasonable assumption, as the contribution of the center-to-limb variation of H I Lyα radiation (a small limb brightening) to the anisotropy of the radiation field can generally be ignored compared to the geometric effects due to the height of the scatterer in the corona. Finally, in the case of anisotropic temperature distributions, the microscopic velocity has the form of a bi-Maxwellian distribution, as initially explored in simulations by Fineschi (2001) and more recently by Khan & Landi Degl'Innocenti (2012).

Given that the corona is an optically thin plasma in the UV, to obtain the emergent signals, we have performed an integration along the line of sight (LOS) of the emission coefficient in Equation (1), and derived for any one of the Stokes parameters, I_i,

$$I_i(\boldsymbol{\Omega}) = \int_{LOS} \epsilon_i(\boldsymbol{\Omega}) ds, \quad (4)$$

where s is the coordinate along the LOS.

3. GBL Model

We adopt the analytic model of Gibson et al. (1996; from here on referred to as GBL) as the basis of our analysis. In general, this analytic solution combines a coronal magnetostatic bulk current (cross-field current) model (Bogdan & Low 1986; Gibson & Bagenal 1995) with stress-free current sheets that appear both at the equator and the boundary of the streamer. This model captures the plasma distribution and magnetic field of the solar corona during solar minimum, in comparison to observations of white-light coronagraphs. Because Gibson et al. (1996) found that the bulk currents played a minimal role in redistributing the plasma, for the purpose of our analysis, we simplify the model to only consider current sheets. In this case, we can describe the background pressure and density in terms of hydrostatic balance. The scale height of these hydrostatic equilibria differs in closed versus open regions, with the current sheets providing a jump in magnetic pressure that balances the jump in thermal pressure such that total pressure is continuous.

For the purposes of the present study, we modify the pressure and density profiles assumed in Gibson et al. (1996) to be more consistent with the observed pressure and density from UVCS. In particular, for the closed region, we assume a semiempirical temperature model (which is denoted $T_\parallel$, the ion temperature along the magnetic field direction) from Vásquez et al. (2003) and the empirical density model from Cranmer et al. (1999). The density and temperature have a power-law distribution along the radial direction, and the pressure is obtained according to the ideal gas law. In the open region, empirical models of density and temperature are adopted from Cranmer et al. (1999). Further details about our modified GBL model can be found in the Appendix, and the basic plasma–magnetic field distribution is illustrated in Figure 2.

Although the GBL model is magnetostatic, it is an observational fact that there is solar wind flowing out of coronal holes (Hassler et al. 1999; Tu et al. 2005), and we need to consider this velocity in our Doppler dimming analysis. We thus use the velocity profile of Cranmer et al. (1999). The magnitude of the velocity increases with height as defined by this profile, and the direction is along the magnetic field. It implies a sonic point (where sound speed equals the solar wind velocity) at $2R_\odot$. The inclusion of velocity thus introduces lateral forces that are not self-consistently treated in the outer field of view (FOV) of our analysis; however, we do not expect this to affect our conclusions, which holds true for the region below the sonic point.

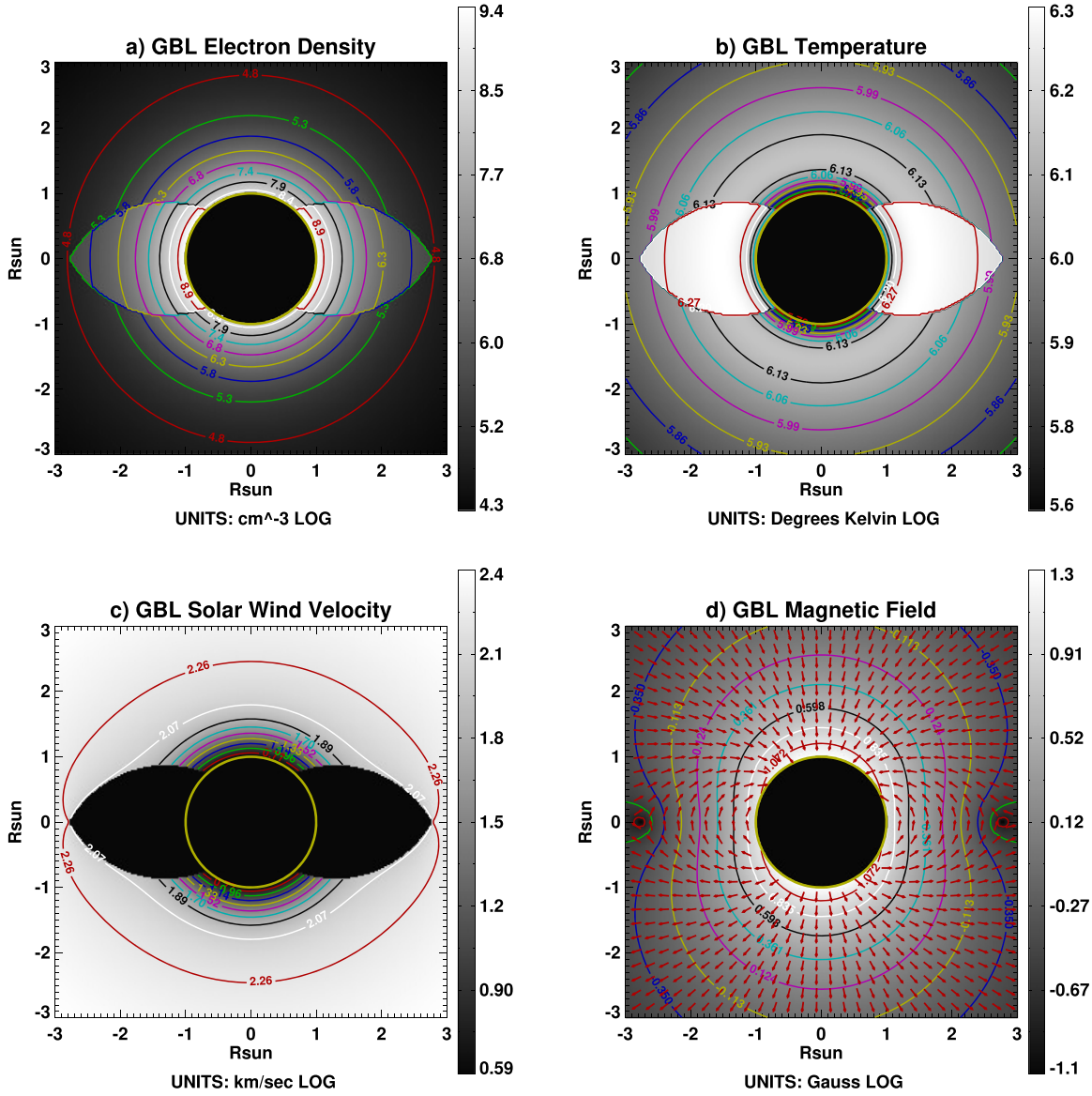

Figure 2. Physical setup from the GBL streamer model. (a) The electron density is high in the streamer and low in the coronal hole. It has a jump at the boundary between the streamer and coronal hole. (b) Temperature is higher in the streamer. It increases near the surface and then decreases when going farther out. (c) The solar wind velocity is only defined in the open region and increases with height. (d) The magnetic field strength is large around the pole and small near the equator, with a jump at the current sheet that balances the jump in thermal pressure. This jump is not apparent in the figure because the corona is magnetically dominated so a small jump in magnetic pressure is sufficient to balance the significant jump in thermal pressure seen in panels (a) and (b). The magnetic field is axisymmetric, and the plane-of-sky (POS) projection of field lines is shown as red arrows.

4. Results

Using the GBL model, we synthesize the polarization signals in the H I Lyα 121.6 nm resonance line by forward-modeling and integrating along the LOS (pointing away from observer into the plane of sky, POS) in a manner similar to Paper I. In this work, the forward calculation is extended to allow the explicit inclusion of the Doppler dimming effect. The solar wind velocity profile that we assumed in Section 3 ranges from a few kilometers per second at the coronal base to hundreds of kilometers per second at the edge of our FOV. Thus, according to Equation (3) in Susino et al. (2018), the Doppler dimming effect increases with higher velocity at larger heights.

In addition, we consider cases where there is anisotropy such that the ratio of temperature perpendicular to the local magnetic field versus temperature parallel to the local magnetic field has a constant value set equal to 2 in the coronal hole (open-field region as shown in Section 3). We have chosen this value based on UVCS measurements (Cranmer 2020). The dimming effect caused by the anisotropic distribution of the microscopic velocity decreases with height, which is an effect of the dipolar magnetic field configuration that becomes more radial at larger heights in the coronal hole.

As in Paper I, we will present the linear polarization fraction ($L/I = \sqrt{Q^2 + U^2}/I$, where I, Q, *and* U are the Stokes parameters integrated across the spectral line) to represent the magnitude of the linear polarization and azimuth ($Az = 0.5 \arctan(U/Q)$) to represent the angle between the linear polarization vector and the local vertical or the radial direction.

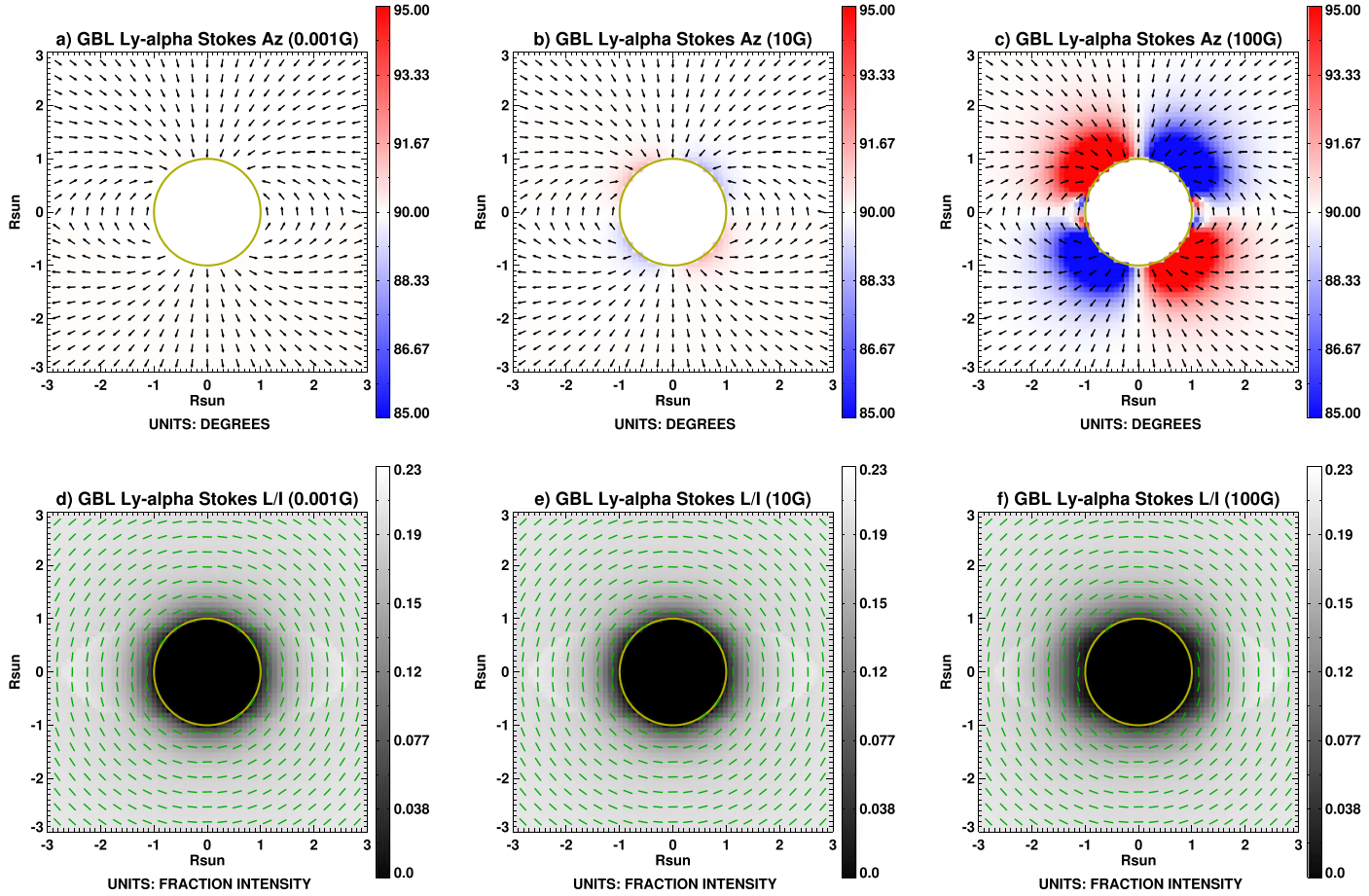

Figure 3. Comparison of azimuth and L/I distribution at H I Lyα with Hanle effect only. The direction of the POS magnetic field is indicated by the black arrows in the top row and the direction of the linear polarization in the bottom row by the green line segments. The overall dipole magnetic field strength from left to right panels is scaled by $\gamma_1 = 0.001$, 10, and 100 G, which can be considered as the field strength at the base of the coronal hole in each panel.

4.1. Magnetic Effects

To start with, we consider the effect of magnetic fields on the emission. The intensity (I) does not change with changes to the magnetic field, but the linear polarization does. The GBL model field is primarily oriented perpendicular to the observer's line of sight; although there is some projection of the magnetic field onto the line of sight for plasma away from the plane of the sky, it is a relatively small effect because the density is highest at the plane of the sky and so this dominates the integration along the line of sight. Thus, the effects on linear polarization are a combination of a geometric effect and the unsaturated Hanle effect as discussed in Paper I.

Figure 3 shows the direction (Az; top) and degree of polarization (L/I; bottom), with the magnetic field increasing from left to right. For reference, the magnetic field direction in the POS is shown as black line segments in the top row, and the linear polarization direction is shown as green line segments in the bottom row. Figure 4 shows a zoomed-in view near the equator. Because the magnetic field in panel (a) is very small (0.001 G), the azimuth is 90° everywhere, or in other words, the linear polarization vector is parallel to the solar limb everywhere. The results with the magnetic field of 0.001 G here and hereafter are treated as baseline references for other cases as shown in the right two columns of Figures 3 and 4, and especially for all the panels in Figure 8 to demonstrate the roles the other two effects (solar wind velocity and temperature anisotropy) play in the linear polarization individually and jointly. As the magnetic field strength becomes large in panels (b) and (c), the linear polarization vector rotates in response to the direction of the magnetic field, and L/I diminishes in the region of the van Vleck angles according to the saturated Hanle effect (see Paper I for a full discussion).

4.2. Solar Wind Doppler Dimming Effect and Effect of Solar Wind Temperature Anisotropy

Figure 5 shows the results for solar wind with isotropic and anisotropic kinetic temperature (hereafter, it will be referred to as isotropic solar wind and anisotropic solar wind for convenience) in the case of a very small magnetic field (0.001 G). Total intensity, L/I, and Az are shown from left to right. The first row ((1a)–(1c)) is for reference, showing a zero-velocity isotropic case. This situation is conceptually sketched in Figure 1, panel (a). On the other hand Figure 1, panel (c) illustrates the results for an isotropic solar wind ((2a)–(2c)). The anisotropic case with zero velocity (no solar wind; (3a)–(3c)) and an anisotropic solar wind ((4a)–(4c)) are shown in the following rows of Figure 5 and schematically illustrated by Figure 1, panels (c) and (d), respectively. To further investigate the differences in these four cases, we select points along a radial cut at 30° colatitude and forward-model I, L/I, Az (Figure 6) from $1R_\odot$ to $3R_\odot$. The four cases (top to bottom in

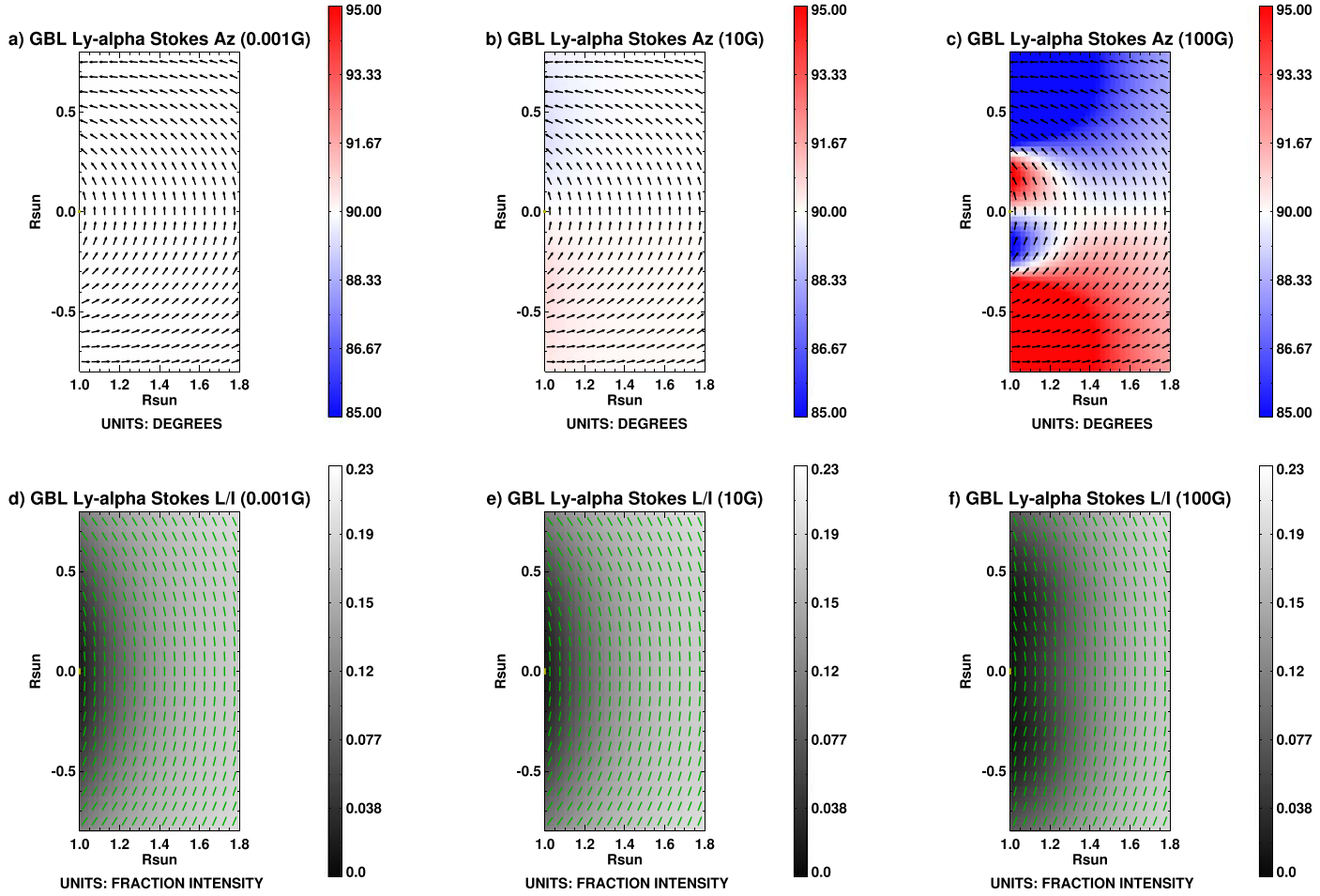

Figure 4. Zoom-in plots of Figure 3 near the equator.

Figure 5) are shown with orange, green, pink, and purple line curves, respectively. Furthermore, Figure 7 presents these profiles normalized to the reference isotropic case with no velocity.

Figure 5, first column, and Figure 6, panel (a), show that the intensity is similar for all four cases, decreasing with solar radius as the electron density decreases. Figure 7, panel (a), illustrates that for all heights, the isotropic wind/no-wind cases are somewhat higher intensity than anisotropic wind/no-wind cases. At larger heliocentric distances, the difference arising from Doppler dimming begins to dominate, and the solar wind cases (both isotropic and anisotropic) are of lower intensity than the cases without a solar wind. Figure 6, panel (b), is a zoom-in of the higher heights to further illustrate this point.

Figure 5, middle panels, show that the linear polarization fraction (L/I) is sensitive to the jump in density across the current sheet because it affects plasma weighting along the LOS, but that in general L/I does not vary significantly for the four cases. Our reference isotropic case, as shown in the orange line of Figures 6(c)–(f), represents a purely resonant-scattering-driven linear polarization, with the fraction of linear polarization L/I increasing with height and direction of linear polarization (azimuth) everywhere tangent to the limb (90°). The introduction of solar wind velocity increases L/I somewhat at higher heights (compare the teal/purple to orange/pink profiles in Figures 6(d) and 7(c)) due to larger dimming of the total intensity relative to linearly polarized light.

The azimuth in these four cases has very different distributions, however. For isotropic zero velocity (Figure 5, panel (1c)), the azimuth is 90° everywhere. For an isotropic solar wind (Figure 5, panel (2c)), the azimuth is greater than 90° along the right diagonal of the FOV and less than 90° along the left one, meaning that the linear polarization vector rotates clockwise along the right diagonal of the FOV and counter-clockwise along the left one. For the anisotropic case with no velocity (Figure 5, panel (3c)), the azimuth has an opposite distribution compared to the isotropic solar-wind case, or in other words, the linear polarization vector rotates in an opposite way to the isotropic solar-wind case. The magnitude of the azimuth is also larger in the anisotropic case than in the isotropic solar-wind case, indicating that the azimuth is more sensitive to the anisotropic distribution of ion temperature compared to the Doppler dimming effect from solar wind velocity assumed in our forward model. In the anisotropic solar-wind case (Figure 5m panel (4c)), the azimuth is modified by a combination of the effects shown in Figure 5, panels (2c) and (3c). At lower heights where the solar wind velocity is small, the azimuth has a distribution like the anisotropic case (Figures 6(e) and 7(d)), while at higher heights where the velocity begins to dominate, the distribution is more like the one in the isotropic solar-wind case (Figures 6(f) and 7(e)).

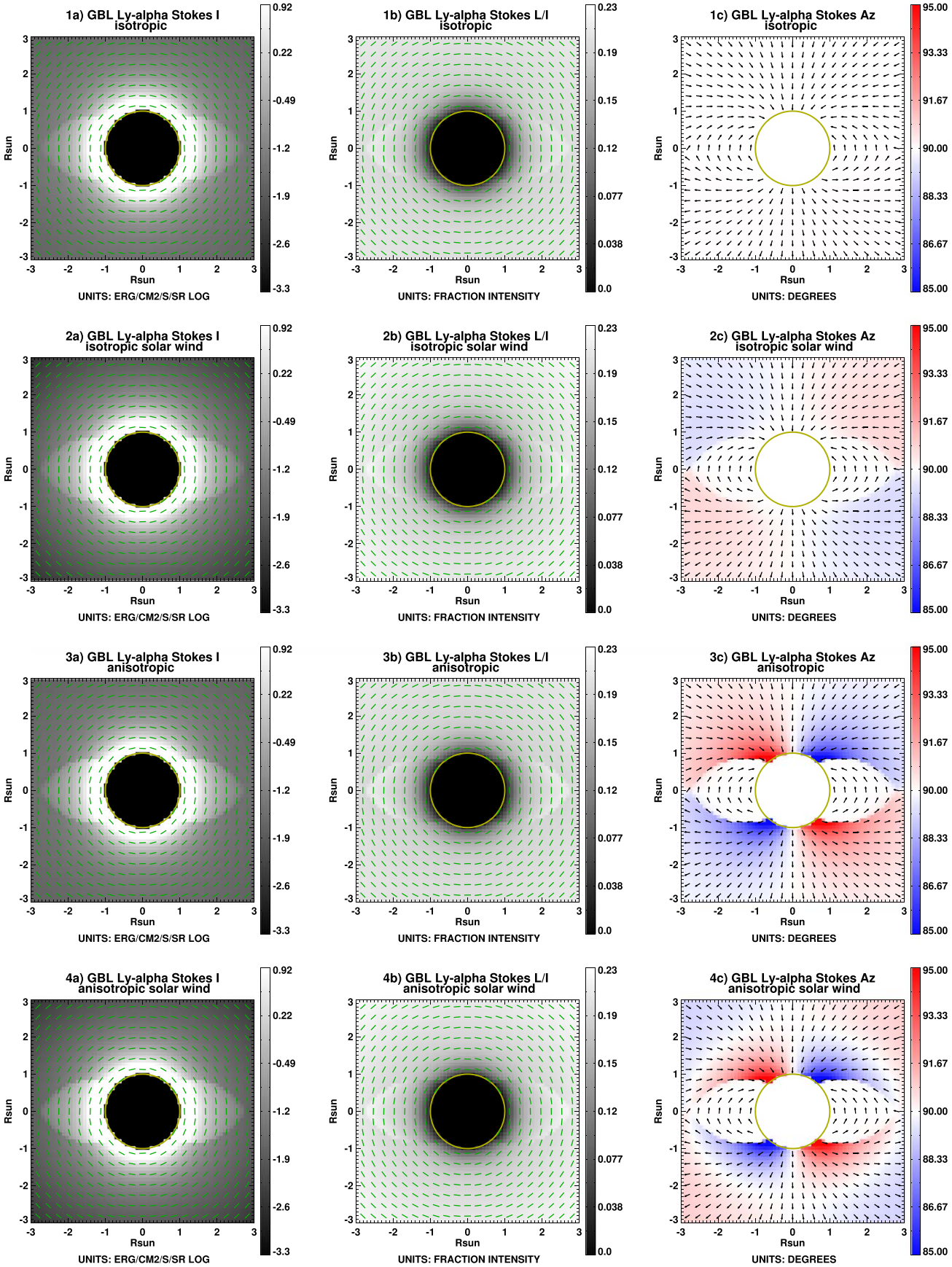

Figure 5. Total intensity (left column), linear polarization fraction (middle column), and azimuth (right column) are synthesized in H I Lyα with a very small (0.001 G) magnetic field. The isotropic case, the isotropic solar wind case, the anisotropic case, and the anisotropic solar wind case are displayed from top to bottom. The overlaid green line segments in the left two columns show the linear polarization direction, and the black line segments in the right column show the direction of the magnetic field.

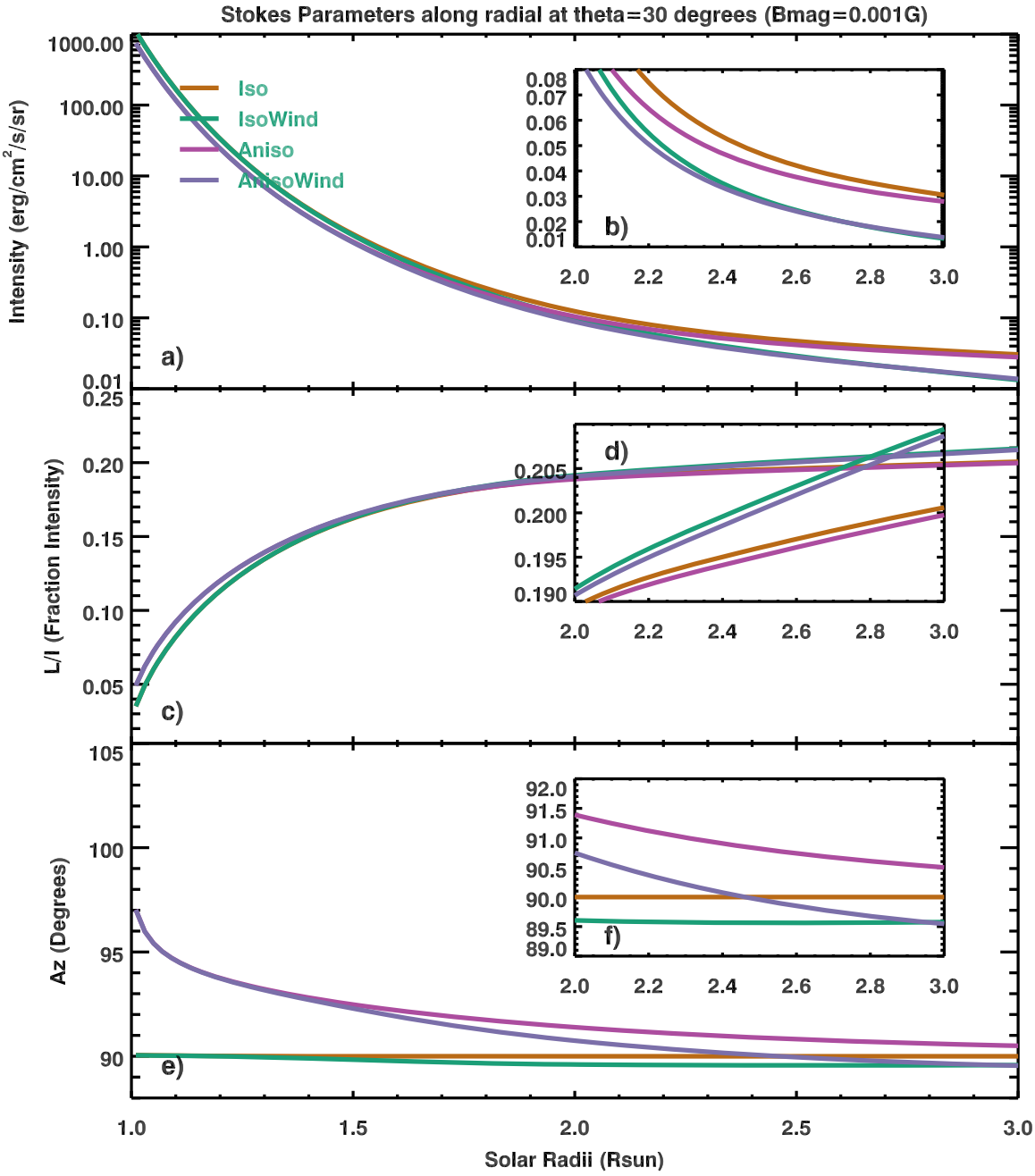

Figure 6. Intensity, linear polarization fraction, and azimuth in the coronal hole from $1R_\odot$ to $3R_\odot$ at a latitude of 30° with a small magnetic field. The isotropic case, the isotropic solar wind case, the anisotropic case, and the anisotropic solar wind case are shown in orange, green, pink, and purple, respectively. The small plots inside each panel are the zoom-in plots from $2R_\odot$ to $3R_\odot$ for the corresponding parameters.

4.3. Syntheses with All Three Effects Together

In real observations, the magnetic Hanle effect, solar wind Doppler dimming effect, and ion temperature anisotropy effect may take place simultaneously. Figures 8–10 illustrate this for a case with a dipole magnetic field strength of 10 G. Compared to Figures 5–7, the intensity and L/I do not change much.

However, the effect of the magnetic field is evident in the linear polarization direction Az. As was true in the magnetic-field-only cases considered in Section 4.1, the linear polarization vector rotates in a pattern akin to the purely anisotropic case (Figure 5, panel (3c)), but at lower heights. The addition of magnetic fields thus superposes this pattern on the nonmagnetic effects described in Section 4.2. The additional rotation at low heights is also seen in the radial profiles of Az, especially in the isotropic cases of Figure 9, panel (e) (orange and green lines).

5. Discussion and Conclusion

In this work, we have forward-modeled the linearly polarized emission of the H I Lyα line taking into consideration the magnetic, solar wind, and ion temperature anisotropy effects. Our results show that all three effects will produce an observable modification to the linearly polarized light arising from resonant scattering.

In particular, the direction, or azimuth, of the linear polarization shows patterns that diagnose the presence of magnetic fields at heights within a few tenths of a solar radius

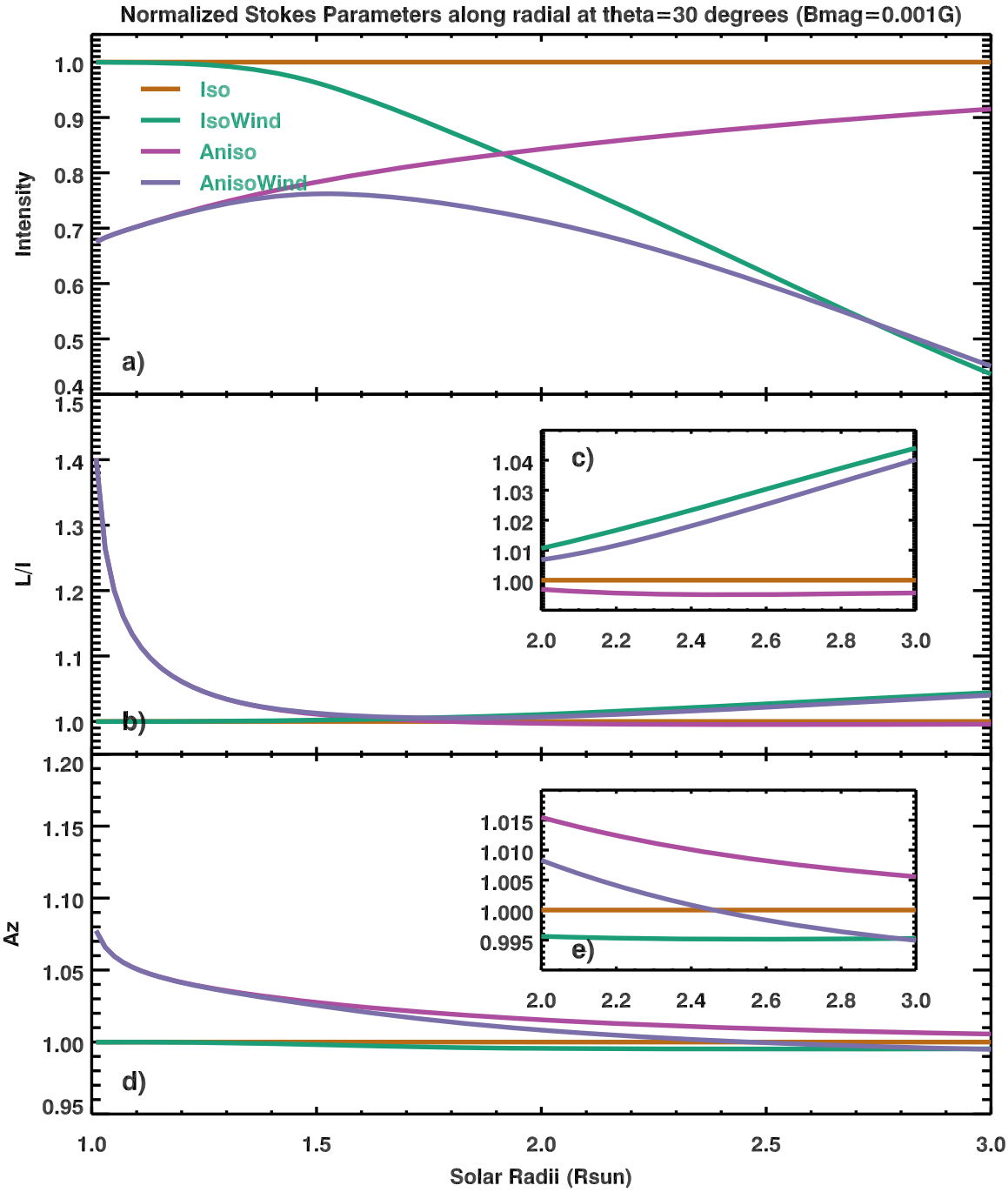

Figure 7. Same as in Figure 6, but are normalized by the reference case (case 1, isotropic).

from the solar surface. In the open-field regions, the linear polarization azimuth is also clearly impacted by the other two effects, with ion temperature anisotropy playing a larger role where the wind speed is not yet fast enough to induce a sizable Doppler dimming effect. This effect, on the other hand, plays a larger role at higher heights where the solar wind begins to dominate. In either case with or without magnetic field, this conversion happens around $2.5R_{\odot}$ at the latitude of 30° under the assumption of the temperature anisotropy equaling 2. These patterns may be oppositely oriented, so the dominance of particular effects at particular heights or magnetic topologies is essential for interpreting observations.

While there are currently existing coronal spectropolarimetric measurements at visible and infrared wavelengths (Lin et al. 2000; Tomczyk et al. 2008; Dima et al. 2019), and observations from the recently completed Daniel K. Inouye Solar Telescope (DKIST) and the future Coronal Solar Magnetic Observatory (COSMO; Tomczyk et al. 2016), there are no UV coronal spectropolarimetry measurements beyond the proof of concept done with the SUMER telescope (Raouafi et al. 1999). Next-generation UV coronagraph instrumentation concepts have been discussed for some time (Kohl et al. 2008). The Solar Probe Analyzer for Ions (SPAN-I) on board the recently launched Parker Solar Probe (PSP; Fox et al. 2016)

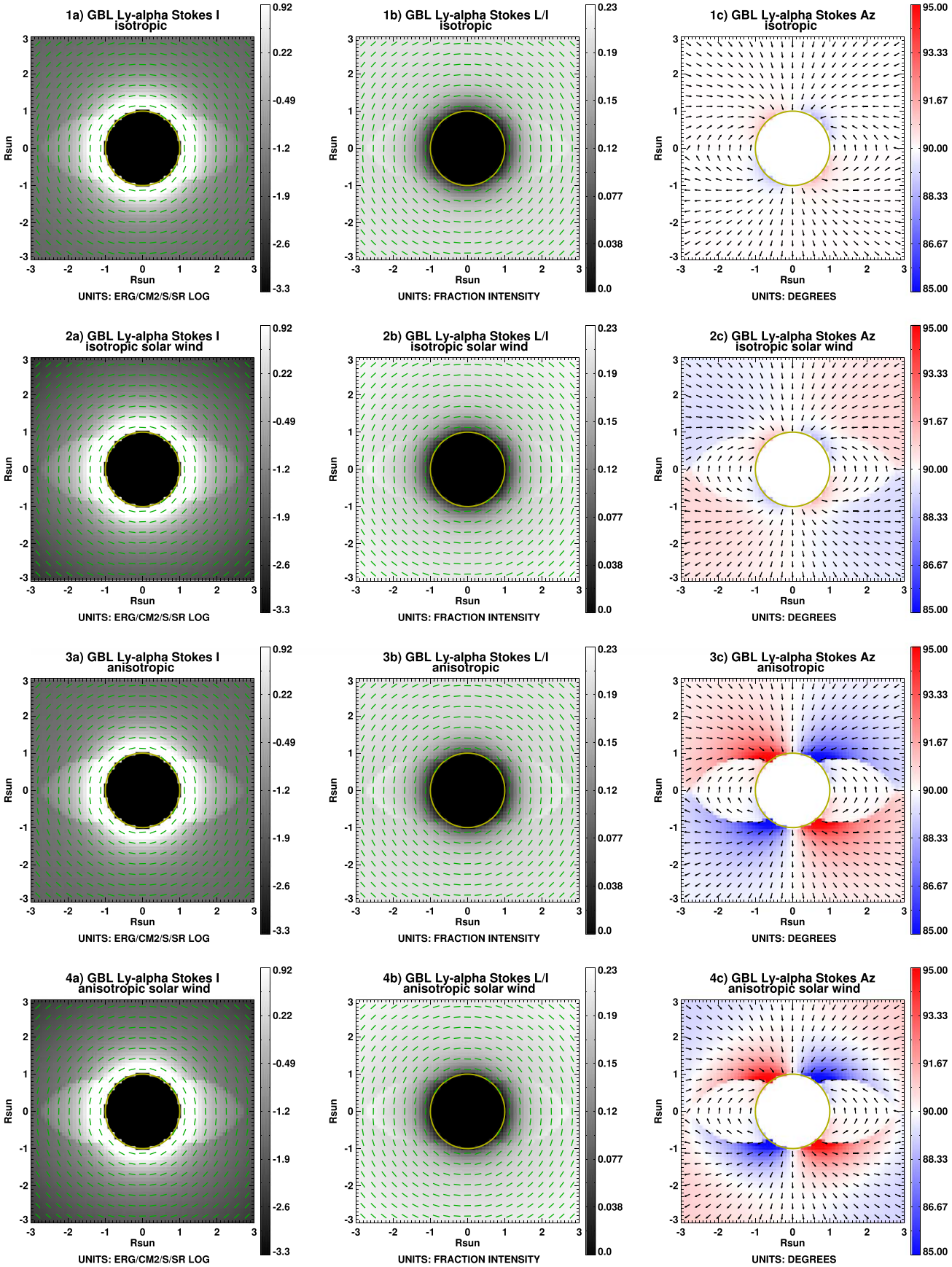

Figure 8. Same as in Figure 5 but with larger magnetic field strength ($\gamma_1 = 10$ G).

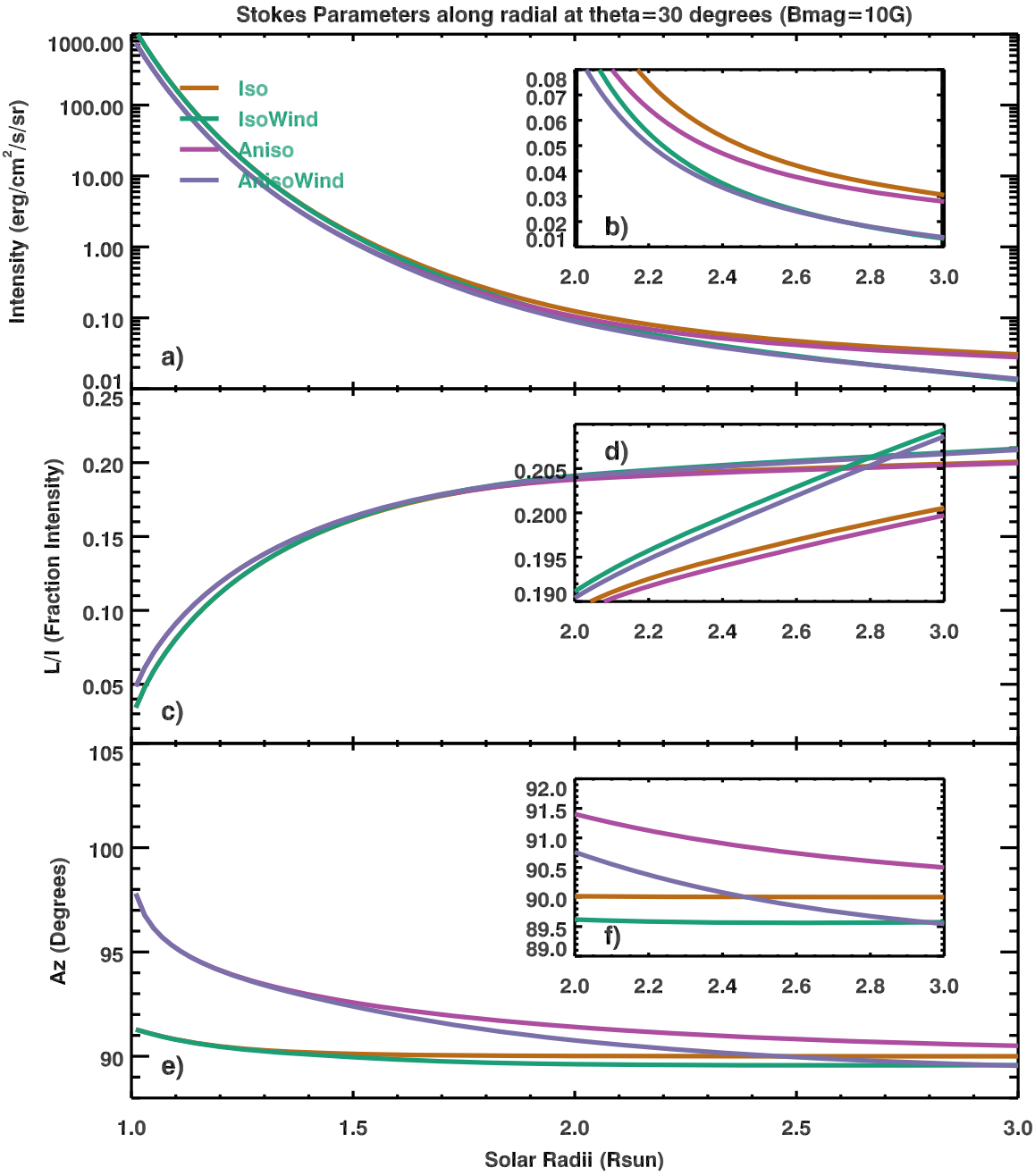

Figure 9. Same as in Figure 6 but with larger magnetic field strength ($\gamma_1 = 10$ G).

measures ion anisotropies in situ in the inner corona, and $T_\perp/T_\parallel$ is found to be 2 at the perihelion (Verniero et al. 2020). The recently launched multiwavelength coronagraph Metis (Romoli et al. 2017) on board the Solar Orbiter as well as the H I Lyα coronagraph on board the China mission of Advanced Space-based Solar Observatory (ASO-S; Gan et al. 2012, 2019; Li 2016; Li et al. 2019), which is scheduled to be launched in 2022, will be able to detect the dimming effects on intensity, although they will not be able to detect linear polarization. The Large Optimized Coronagraph for Key Emission line Research (LOCKYER; Vourlidas et al. 2018) is proposed based on the success of SOHO/UVCS, and some relevant development work has been undertaken (Laming et al. 2019). The analysis presented here motivates the development of future telescopes capable of coronal ultraviolet spectropolarimetry.

In this study, we have shown the potential of UV spectropolarimetry for the diagnostics not only of the coronal magnetic field but also—and this is the novelty—of the degree of anisotropy in the microscopic velocity distributions of coronal ions. This diagnostic is complementary to that based on high-resolution UV spectroscopy as demonstrated by UVCS/SOHO. This study has highlighted an interesting feature of this diagnostic: unlike the Hanle effect of the H I Lyα line, which is sensitive to the magnetic field strengths expected to be found in the corona at heliocentric heights of a few tenths of solar radii, the polarimetric Doppler dimming effect of UV lines is sensitive to solar wind speeds and to kinetic temperature anisotropies in coronal regions at heliocentric heights extending up to a few solar radii.

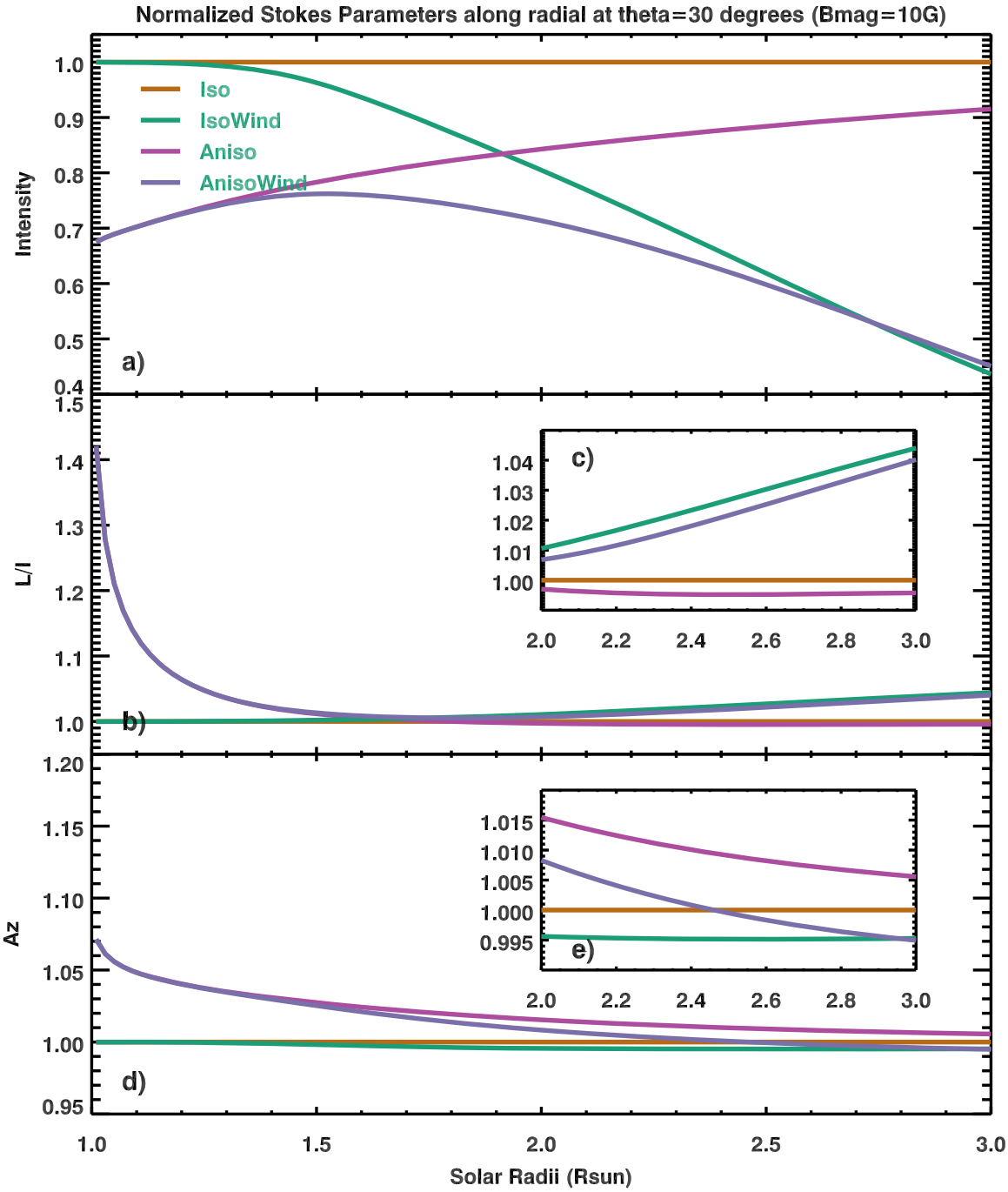

Figure 10. Same as in Figure 7 but with larger magnetic field strength ($\gamma_1 = 10$ G).

We plan to extend the analyses presented here and in Paper I to include more globally complex and self-consistent 3D MHD simulations that include a multifluid solar wind model considering the different properties and interactions of electrons, protons, and heavy ions (e.g., Ofman 2019) in preparation for this and other future UV spectropolarimetric missions.

J.Z. is a visiting postdoc at HAO, supported by the Chinese Scholarship Council (CSC NO. 201704910457). This work is also supported by the National Natural Science Foundation of China, grant Nos. 11503089 and U1731241, and the Chinese Academy of Science Strategic Pioneer Program on Space Science, grant Nos. XDA15052200, XDA15320103, and XDA15320301. The National Center for Atmospheric Research is a major facility sponsored by the National Science Foundation under cooperative agreement No. 1852977. This work was further supported by the Air Force Office of Scientific Research grant FA9550-15-1-0030. L.O. acknowledges support by NASA cooperative agreement NNG11PLA10A2 to CUA and travel support by HAO/UCAR. S.F. is an Affiliate Scientist of HAO/NCAR. S.F. and R.S. acknowledge support by the Visitor Program at HAO.

Appendix

The Gibson–Bagenal–Low (GBL) model (Gibson et al. 1996) is an analytic solution for magnetostatic equilibrium as follows:

$$\frac{1}{4\pi}(\nabla \times \boldsymbol{B}) \times \boldsymbol{B} - \nabla P - \rho\frac{GM}{r^2}\hat{r} = 0, \tag{A1}$$

in which the Lorentz force from a magnetic field and the forces from thermal pressure gradients and gravity are balanced. This solution constructs a streamer that has a density and pressure jump at the boundary between closed and open fields that is kept in total pressure continuity via a jump in magnetic field strength, i.e., introducing a stress-free current sheet at the closed–open-field interface.

In this paper, we have both simplified and modified the GBL model as presented in Gibson et al. (1996). We have simplified it first by considering only a dipole magnetic field, as opposed to a combination of dipole and octupole field terms. Second, we do not consider volume currents but only current sheets around the open-/closed-field region and at the equator.

We have modified the model in the following way. Gibson et al. (1996) defined a parameter $C_{\rm open}$ to control the jump condition for magnetic and gas pressure at the closed-/open-field interface. In particular, the magnetic field in the open region was increased by a factor of $C_{\rm open} > 1$ relative to the magnetic field in the closed region ($\boldsymbol{B}_{\rm closed}$; defined by parameters controlling the dipole and octupole magnetic components), while the spherically symmetric pressure distribution in the open region was decreased by the addition of a (negative) quantity:

$$\Delta P = (1 - C_{\rm open}^2)\frac{\boldsymbol{B}_{\rm closed}^2}{8\pi}. \tag{A2}$$

The spherically symmetric density distribution was similarly decreased in a manner that satisfied hydrostatic equilibrium. In this paper, we chose instead to explicitly define spherically symmetric, hydrostatically balanced density/pressure distributions for both the open and closed regions. The jump condition $C_{\rm open}(r)$ thus is defined by the change in gas pressure across the open/closed boundary and the magnetic field increased by this factor as above.

In particular, we have chosen the form of the spherically symmetric density models as follows:

$$\rho = n_1 \cdot 10^5 \cdot n_2 \cdot \left(\frac{1}{r}\right)^{n_3} + n_4 \cdot \left(\frac{1}{r}\right)^{n_5}. \tag{A3}$$

The pressure is determined by combining the ideal gas law with a spherically symmetric temperature model, i.e.,

$$T = \frac{10^6}{(t_1 \cdot r^{t_2} + t_3 \cdot r^{t_4})}. \tag{A4}$$

In the closed region, we set the parameters $[n_1, n_2, n_3, n_4, n_5] = [6.0, 3890, 10.5, 8.69, 2.57]$, following Cranmer et al. (1999), and $[t_1, t_2, t_3, t_4] = [0.33, 0.55, 0.67, -6.6]$ following Vásquez et al. (2003). In the open region, we set the parameters $[n_1, n_2, n_3, n_4, n_5, t_1, t_2, t_3, t_4] = [1.0, 3890, 10.5, 8.69, 2.57, 0.35, 1.1, 1.9, -6.6]$, following Cranmer et al. (1999).

Finally, although not part of the GBL magnetostatic model, we include outflow in the open-field regions in our forward-modeling of the H I Lyα emission. For this, we use the following expression from Cranmer et al. (1999) and assume the velocity is parallel to the magnetic field:

$$V = \frac{110 + 445 \cdot \left(1 - \frac{1}{r}\right)^{3.47}}{1 + e^{-6.5\cdot(r-1.5)}}. \tag{A5}$$

One final corrigendum: we need to clarify that there are two typographic errors in the appendix of Gibson et al. (1996), where the last term of Equation (A1) should be $\frac{4}{\pi b}U$, and the last term of Equation (A2) should be $-\frac{12}{45\pi b^3}\eta$. These changes are consistent with Appendix B in Low (1986, Equations (B3) and (B4), taking into consideration differences in normalizations). These corrections and the modifications described above are incorporated in the model function "GIBBAGLOW," which has been added into the FORWARD SolarSoft IDL package (Gibson et al. 2016). Note that GIBBAGLOW allows full implementation of the model allowing volume currents and octupole magnetic configurations.

ORCID iDs

Jie Zhao (赵洁) https://orcid.org/0000-0003-3160-4379
Sarah E. Gibson https://orcid.org/0000-0001-9831-2640
Silvano Fineschi https://orcid.org/0000-0002-2789-816X
Roberto Susino https://orcid.org/0000-0002-1017-7163
Roberto Casini https://orcid.org/0000-0001-6990-513X
Steven R. Cranmer https://orcid.org/0000-0002-3699-3134
Leon Ofman https://orcid.org/0000-0003-0602-6693
Hui Li (黎辉) https://orcid.org/0000-0003-1078-3021

References

Abbo, L., Ofman, L., Antiochos, S. K., et al. 2016, SSRv, 201, 55
Antonucci, E., Abbo, L., & Telloni, D. 2012, SSRv, 172, 5
Antonucci, E., Giordano, S., & Dodero, M. A. 2000, AdSpR, 25, 1923
Bąk-Stęślicka, U., Gibson, S. E., Fan, Y., et al. 2013, ApJL, 770, L28
Beckers, J. M., & Chipman, E. 1974, SoPh, 34, 151
Bogdan, T. J., & Low, B. C. 1986, ApJ, 306, 271
Bommier, V., & Sahal-Bréchot, S. 1982, SoPh, 78, 157
Chandran, B. D. G., Li, B., Rogers, B. N., Quataert, E., & Germaschewski, K. 2010, ApJ, 720, 503
Cranmer, S. R. 2001, JGR, 106, 24937
Cranmer, S. R. 2014, ApJS, 213, 16
Cranmer, S. R. 2020, ApJ, 900, 105
Cranmer, S. R., Kohl, J. L., Noci, G., et al. 1999, ApJ, 511, 481
Cranmer, S. R., Panasyuk, A. V., & Kohl, J. L. 2008, ApJ, 678, 1480
Davila, J. M., & Ofman, L. 1999, SSRv, 87, 165
Dima, G. I., Kuhn, J. R., & Schad, T. A. 2019, ApJ, 877, 144
Dolei, S., Spadaro, D., & Ventura, R. 2016, A&A, 592, A137
Domingo, V., Fleck, B., & Poland, A. I. 1995, SSRv, 72, 81
Fineschi, S. 2001, in ASP Conf. Ser. 248, Magnetic Fields Across the Hertzsprung–Russell Diagram, ed. G. Mathys, S. K. Solanki, & D. T. Wickramasinghe (San Francisco, CA: ASP), 597
Fineschi, S., Hoover, R. B., Fontenla, J. M., & Walker, A. B. C. 1991, OptEn, 30, 1161
Fineschi, S., Hoover, R. B., Zukic, M., et al. 1993, Proc. SPIE, 1742, 423
Fineschi, S., van Ballegoijen, A., & Kohl, J. L. 1999, in ESA Special Publication 446, 8th SOHO Workshop: Plasma Dynamics and Diagnostics in the Solar Transition Region and Corona, ed. J. C. Vial & B. Kaldeich-Schü (Paris: ESA), 317
Fox, N. J., Velli, M. C., Bale, S. D., et al. 2016, SSRv, 204, 7
Gan, W., Huang, Y., & Yan, Y. 2012, SSPMA, 42, 1274
Gan, W.-Q., Zhu, C., Deng, Y.-Y., et al. 2019, RAA, 19, 156
Gary, S. P., Yin, L., Winske, D., et al. 2003, JGRA, 108, 1068
Gary, S. P., Yin, L., Winske, D., & Ofman, L. 2001, JGR, 106, 10715
Gibson, S., Kucera, T., White, S., et al. 2016, FrASS, 3, 8
Gibson, S. E., & Bagenal, F. 1995, JGR, 100, 19865
Gibson, S. E., Bagenal, F., & Low, B. C. 1996, JGR, 101, 4813
Gibson, S. E., Dalmasse, K., Rachmeler, L. A., et al. 2017, ApJL, 840, L13
Hassler, D. M., Dammasch, I. E., Lemaire, P., et al. 1999, Sci, 283, 810

Hyder, C. L., & Lites, B. W. 1970, SoPh, 14, 147
Isenberg, P. A., Vasquez, B. J., & Hollweg, J. V. 2019, ApJ, 870, 119
Khan, A. 2012, A&A, 545, A52
Khan, A., Belluzzi, L., Landi Degl'Innocenti, E., Fineschi, S., & Romoli, M. 2011, A&A, 529, A12
Khan, A., & Landi Degl'Innocenti, E. 2012, A&A, 543, A158
Kohl, J. L., Esser, R., Gardner, L. D., et al. 1995, SoPh, 162, 313
Kohl, J. L., Jain, R., Cranmer, S. R., et al. 2008, JApA, 29, 321
Kohl, J. L., Noci, G., Antonucci, E., et al. 1997, SoPh, 175, 613
Kohl, J. L., Noci, G., Antonucci, E., et al. 1998, ApJL, 501, L127
Kohl, J. L., Noci, G., Cranmer, S. R., & Raymond, J. C. 2006, A&ARv, 13, 31
Laming, J. M., Vourlidas, A., Korendyke, C., et al. 2019, ApJ, 879, 124
Landi Degl'Innocenti, E. 1984, SoPh, 91, 1
Landi Degl'Innocenti, E. 1985, SoPh, 102, 1
Landi Degl'Innocenti, M., & Landi Degl'Innocenti, E. 1988, A&A, 192, 374
Li, B., Li, X., Hu, Y.-Q., & Habbal, S. R. 2004, JGRA, 109, A07103
Li, H. 2016, in IAU Symp. 320, Solar and Stellar Flares and their Effects on Planets, ed. A. G. Kosovichev, S. L. Hawley, & P. Heinzel (Cambridge: Cambridge Univ. Press), 436
Li, H., Chen, B., Feng, L., et al. 2019, RAA, 19, 158
Li, X., Habbal, S. R., Kohl, J. L., & Noci, G. 1998, ApJL, 501, L133
Lin, H., Kuhn, J. R., & Coulter, R. 2004, ApJL, 613, L177
Lin, H., Penn, M. J., & Tomczyk, S. 2000, ApJL, 541, L83
Low, B. C. 1986, ApJ, 310, 953
Maneva, Y. G., Ofman, L., & Viñas, A. 2015, A&A, 578, A85
Maneva, Y. G., ViñAs, A. F., & Ofman, L. 2013, JGRA, 118, 2842
McComas, D. J., Ebert, R. W., Elliott, H. A., et al. 2008, GeoRL, 35, L18103
Ofman, L. 2010, JGRA, 115, A04108
Ofman, L. 2019, SoPh, 294, 51
Ofman, L., & Davila, J. M. 2001, ApJ, 553, 935
Ofman, L., Davila, J. M., Nakariakov, V. M., & ViñAs, A. F. 2005, JGRA, 110, A09102
Ofman, L., Gary, S. P., & ViñAs, A. 2002, JGRA, 107, 1461
Ofman, L., Viñas, A., & Gary, S. P. 2001, ApJL, 547, L175
Ofman, L., & ViñAs, A. F. 2007, JGRA, 112, A06104
Ofman, L., Viñas, A. F., & Maneva, Y. 2014, JGRA, 119, 4223
Raouafi, N. E., Lemaire, P., & Sahal-Bréchot, S. 1999, A&A, 345, 999
Raouafi, N. E., Sahal-Bréchot, S., & Lemaire, P. 2002a, A&A, 396, 1019
Raouafi, N. E., Sahal-Bréchot, S., Lemaire, P., & Bommier, V. 2002b, A&A, 390, 691
Raouafi, N. E., & Solanki, S. K. 2006, A&A, 445, 735
Romoli, M., Landini, F., Antonucci, E., et al. 2017, Proc. SPIE, 10563, 105631M
Sahal-Bréchot, S., Malinovsky, M., & Bommier, V. 1986, A&A, 168, 284
Sahal-Bréchot, S., & Raouafi, N. E. 2006, A&A, 445, 681
Susino, R., Bemporad, A., Jejčič, S., & Heinzel, P. 2018, A&A, 617, A21
Titov, V. S., & Démoulin, P. 1999, A&A, 351, 707
Titov, V. S., Hornig, G., & Démoulin, P. 2002, JGRA, 107, 1164
Tomczyk, S., Card, G. L., Darnell, T., et al. 2008, SoPh, 247, 411
Tomczyk, S., Landi, E., Burkepile, J. T., et al. 2016, JGRA, 121, 7470
Tu, C. Y., & Marsch, E. 2002, JGRA, 107, 1249
Tu, C.-Y., Zhou, C., Marsch, E., et al. 2005, Sci, 308, 519
Vásquez, A. M., van Ballegooijen, A. A., & Raymond, J. C. 2003, ApJ, 598, 1361
Verniero, J. L., Larson, D. E., Livi, R., et al. 2020, ApJS, 248, 5
Vourlidas, A., Ko, Y. K., Laming, J. M., Korendyke, C., & Strachan, L. 2018, AGUFM, 2018, SH34A-02
Zhao, J., Gibson, S. E., Fineschi, S., et al. 2019, ApJ, 883, 55